Weierstraß–Institut
für Angewandte Analysis und Stochastik

im Forschungsverbund Berlin e.V.

Landau–Ginzburg Model for a Deformation–Driven Experiment on Shape Memory Alloys

Nikolaus Bubner

submitted: 13th September 1995

Weierstraß–Institut
für Angewandte Analysis
und Stochastik
Mohrenstraße 39
D – 10117 Berlin
Germany

Preprint No. 171
Berlin 1995

Edited by
Weierstraß–Institut für Angewandte Analysis und Stochastik (WIAS)
Mohrenstraße 39
D — 10117 Berlin
Germany

Fax: + 49 30 2044975
e–mail (X.400): c=de;a=d400-gw;p=WIAS-BERLIN;s=preprint
e–mail (Internet): preprint@wias-berlin.de

Landau–Ginzburg Model for a Deformation–Driven Experiment on Shape Memory Alloys

Nikolaus Bubner

Weierstrass Institute for Applied Analysis and Stochastics, Mohrenstr. 39, 10117 Berlin, FRG

Abstract

A Landau–Ginzburg model describing first order martensitic phase transitions in shape memory alloys is considered. The model developed by Falk is transformed in order to simulate deformation–driven experiments done by I. Müller and his co–workers. In these experiments, they do not only observe load–deformation hysteresis loops but also small loops inside these hysteresis loops. Numerical simulations for a CuZnAl single crystal show good agreement with the experiment. We find, for example, nucleation processes, moving phase boundaries, rate–independent hysteresis loops and, for the first time, interior loops.

1 Introduction

Shape memory alloys[1] (SMA) have received increasing attention in recent years partly due to the wide range of their technical applicability in active structures. They show a noticeable change in their mechanical behaviour, i.e. stress–strain relation in different temperature ranges: elastic at high temperatures and pseudo– or quasiplastic at low temperatures. An alloy can be permanently deformed (up to 10%) without fracture and recovers its old shape under heating or cooling. This is the so–called shape memory effect. It is due to first order structural phase transitions between different equilibrium configurations of the metallic lattice, named austenite and martensite. Austenite is

[1] CuZnAl, AuCuZn, NiTi, ...

the undeformed crystal lattice which is stable at high temperatures. By deforming the lattice, one obtains 24 crystallographically equivalent variants. These martensite variants prevail at low temperatures.

A large number of papers deal with experimental observations, physical modelling, mathematical investigation and numerical simulations, such as [FA1,FA2,FA3,WIL,RO, HM,FHM,SP,NS,KL] to name only a few. Here, we transfer the model developed by Falk [FA1,FA2,FA3,SP] for load– and temperature–driven experiments to deformation–driven ones (see Figure 1). A thin rod of a SMA is clamped on one side, and on the other side it is pulled and pushed in the course of time by an elongation $m(t)$. The numerical scheme of [NS,KL] is modified to simulate an experiment for a CuZnAl single crystal done by [GL]. We show the results obtained by [BU]. The mathematical investigation (local and global existence, uniqueness, control problem) also given in that work will be presented in a forthcoming paper.

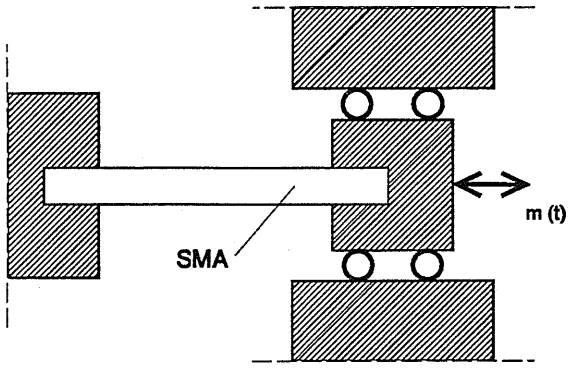

Figure 1: Deformation–Driven Experiment

2 The model

Falk considers a one–dimensional problem. In this case of a thin rod, we only have two variants of martensite, called $M+$ and $M-$ (see Figure 2). The momentum balance here reads

$$\rho u_{tt} - \sigma_x + \mu_{xx} = 0, \tag{2.1}$$

where ρ is the constant mass density[2], u the displacement perpendicular to the rod, σ the stress in the rod, and μ the couple stress. One takes the couple stress into account because the lattice curvature due to the different phases of the rod should not be neglected. The temperature depending on the stress, Falk also considers the energy balance (see also [STO]):

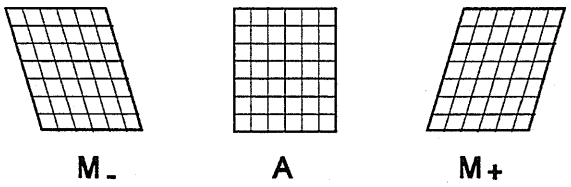

Figure 2: M_-, A, and M_+

$$\rho e_t + q_x - \sigma u_{xt} - \mu u_{xxt} = g. \tag{2.2}$$

[2]The change in volume due to the phase transitions is negligible.

Here, e denotes the specific internal energy, q the heat flux, u_x the shear strain (perpendicular to the rod) and g the density of heat sources and sinks. Taking a specific free energy F, the thermodynamic relations

$$s = -\frac{\partial F}{\partial \theta}, \qquad e = F + \theta s = F - \theta \frac{\partial F}{\partial \theta}, \tag{2.3}$$

and Fourier's law for the heat flux ($q = -\kappa \theta_x$; θ denotes the absolute temperature and κ the thermal heat conductivity), one can show that the Clausius–Duhem–Inequality

$$\rho s_t \geq -\left(\frac{q}{\theta}\right)_x + \frac{g}{\theta} \tag{2.4}$$

is complied with if one chooses:

$$\sigma = \rho \frac{\partial F}{\partial u_x} \quad \text{and} \quad \mu = \rho \frac{\partial F}{\partial u_{xx}}; \tag{2.5}$$

s is the specific entropy.

Now, a Landau–Devonshire ansatz is chosen to describe the first order phase transitions. In order to model the energy stored between different phases, a term containing the gradient of the strain is added to the free energy. It is the change of the strain which has to be penalised in some way, the most simple possibility being δu_{xx}^2, $\delta > 0$, the so–called Ginzburg–term, δ being the Ginzburg–coefficient. So, we have the following free energy density:

$$\tilde{F}(u_x, u_{xx}, \theta) = \tilde{F}_0(\theta) + \frac{\gamma}{2}(\theta - \theta_1)u_x^2 - \frac{\beta}{4}u_x^4 + \frac{\alpha}{6}u_x^6 + \frac{\delta}{2}u_{xx}^2; \tag{2.6}$$

α, β, γ, and θ_1 are material constants which have to be determined for each specimen. Below θ_1, austenite is unstable. A typical form of $\tilde{F}_0(\theta)$ is:

$$\tilde{F}_0(\theta) = -c_e\, \theta \log\left(\frac{\theta}{\tilde{\theta}}\right) + c_e\, \theta + C, \tag{2.7}$$

where c_e is the specific heat, $\tilde{\theta}$ a material constant, and C is a constant to be chosen. Thus, for high temperatures, we find that $\tilde{F}(., u_{xx}, \theta)$ becomes convex, only austenite is stable, and

$$\sigma(u_x, \theta) = \frac{\partial \tilde{F}}{\partial u_x} = \gamma(\theta - \theta_1)u_x(x,t) - \beta u_x^3(x,t) + \alpha u_x^5(x,t) \tag{2.8}$$

becomes a strictly increasing function: the rod shows an elastic behaviour. Low temperatures show $\tilde{F}(., u_{xx}, \theta)$ with two minima (only $M+$ and $M-$ are stable) at $u_x = \pm m_0 > 0$, $\sigma(., \theta)$ is shown in Figure 3. We refer to this as ferro– or quasiplasticity.

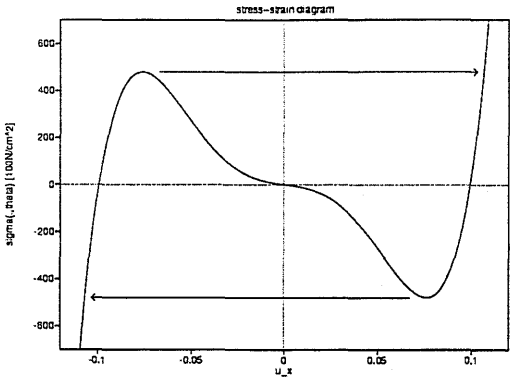

Figure 3: stress–strain relation for low temperatures

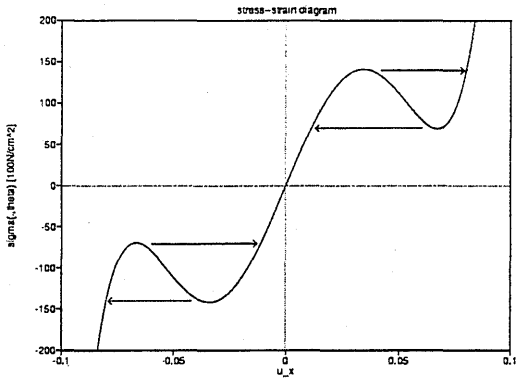

Figure 4: stress–strain relation for intermediate temperatures

A hysteresis is obtained by following the lines indicated by the arrows. In an intermediate temperature range, we have a pseudoelastic behaviour shown in Figure 4. All phases may occur. So, the linearized strain $\varepsilon := u_x$ plays the part of the order parameter: $\varepsilon \approx 0$: austenite; $\varepsilon \approx \pm m_0 : M\pm$ (m_0 depends on the material).

In three space dimensions, however, a force acting on the lattice leads to strains in all spatial directions. Considering an intersection of two dimensions, one obtains schematically what is depicted in Figure 5. We now look into the displacement field $\vec{u}$ as having two components which themselves depend only on one coordinate, i.e. x. Up to now, the displacement component perpendicular to the rod was investigated, in the above mentioned papers. For instance, they simulated a rod clamped on both sides and looked into phase transitions due to temperature changes or a force acting perpendicularly on the rod. In order to simulate an experiment where the phase transitions are caused by an elongation $m(t)$ at one side of the rod, we examine the displacement *in* the direction of the rod. Since it is a one–dimensional approach, it still depends on x only. Thus, it turns out that the order parameter is no longer the shear strain $\varepsilon = \frac{\partial u^{(y)}}{\partial x}$ ((y) indicates the spatial direction, see Figure 5) but the strain $\varepsilon = \frac{\partial u^{(x)}}{\partial x}$ *in* the direction of the elongation $m(t)$ which is

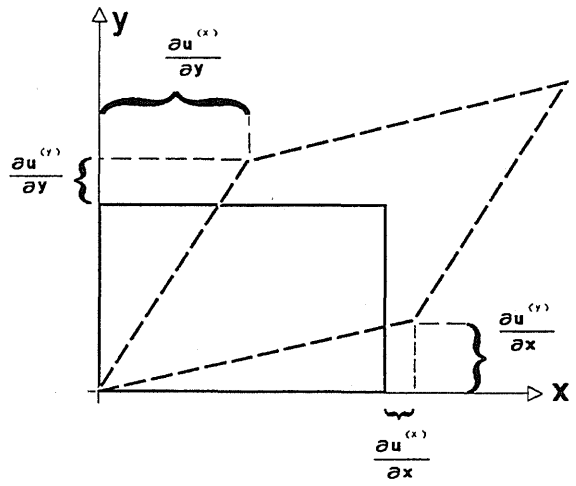

Figure 5: Deformed crystal (see [MM])

called the *deformation*. This means that the momentum balances for x and y decouple:

$$f^{(x)} = \frac{\partial \sigma^{(x)}}{\partial x} + \underbrace{\frac{\partial \tau_{xy}}{\partial y}}_{=0} = \rho u_{tt}^{(x)} + \mu_{xx}^{(x)}, \tag{2.9}$$

$$f^{(y)} = \frac{\partial \tau_{yx}}{\partial x} + \underbrace{\frac{\partial \sigma^{(y)}}{\partial y}}_{=0} = \rho u_{tt}^{(y)} + \mu_{xx}^{(y)}, \tag{2.10}$$

where

$$\sigma = \begin{pmatrix} \sigma^{(x)} & \tau_{xy} \\ \tau_{yx} & \sigma^{(y)} \end{pmatrix} \tag{2.11}$$

is the symmetric stress tensor. Equation (2.10) has been concentrated on up to this point; now we apply equation (2.9). We end up with a structure of the system comparable to the one before, but the meanings of the physical quantities have partly changed: u (that is $u^{(x)}$ in (2.9); in the sequel we will only refer to this direction, so for simplicity we continue omitting the index) is now the displacement *in* the direction of the rod, i.e. the difference between the initial state and the elongated one. All that has been said about the former model is valid for this one, too. The material constant m_0 may have another value.

Choosing the length of the rod $l := 1$, we have the following boundary conditions:

$$u(0,t) = 0, \qquad u(1,t) = m(t). \tag{2.12}$$

Furthermore, we do not wish to prescribe any strain on the boundary, so we choose

$$u_{xx}(0,t) = u_{xx}(1,t) = 0. \tag{2.13}$$

There is an initial state $u(0,x) = u_0(x)$, and the initial velocity will be

$$u_t(0,x) = u_1(x) = 0. \tag{2.14}$$

In the experiment, the rod is in a bath, meaning that all the latent heat which may occur is immediately absorbed; the experiment is isothermal. The energy balance is essential in our model, we do not want to neglect it by taking $\theta = \text{const.}$ and looking only into the momentum balance. Also, g can be taken as a control variable as well as m or the outside temperature θ_Γ. In order to simulate the experiment, we take

$$-\kappa\theta_x(1,t) = \bar{\kappa}(\theta(1,t) - \theta_\Gamma(t)), \qquad \theta_x(0,t) = 0, \tag{2.15}$$

as boundary conditions for the energy balance. Choosing the heat exchange coefficient $\bar{\kappa}$ big enough, we have an isothermal behaviour of our system at $x = 1$. Thus, we can

compare physical quantities at $x = 1$ (such as σ) with the experimental data. We are aware of the fact that the Falk model was developed in order to describe the dynamical behaviour in contrast to this quasistatic experiment. We will come back to this while discussing the numerical results in the last section.

Summarizing, we have the following system ($\Omega := (0,1)$, $\Omega_T := \Omega \times (0,T)$):

$$\begin{aligned}
\rho u_{tt} &- (\gamma(\theta-\theta_1)u_x - \beta u_x^3 + \alpha u_x^5)_x + \delta u_{xxxx} = 0, \quad \text{in} \quad \Omega_T, && \text{(2.16a)}\\
c_e\theta_t &- \kappa\theta_{xx} - \gamma\theta u_x u_{xt} = g(x,t), \quad \text{in} \quad \Omega_T, && \text{(2.16b)}\\
u(0,t) &= u_{xx}(0,t) = u_{xx}(1,t) = 0, \quad u(1,t) = m(t), \quad \forall t \in [0,T], && \text{(2.16c)}\\
\theta_x(0,t) &= 0, \quad -\kappa\theta_x(1,t) = \bar{\kappa}(\theta(1,t) - \theta_\Gamma(t)), \quad \forall t \in [0,T], && \text{(2.16d)}\\
u(x,0) &= u_0(x), \quad u_t(x,0) = 0, \quad \forall x \in \overline{\Omega}, && \text{(2.16e)}\\
\theta(x,0) &= \theta_0(x), \quad \forall x \in \overline{\Omega}. && \text{(2.16f)}
\end{aligned}$$

We can prove [BU] that this system has a unique classical solution such that θ remains positive for any time $T > 0$.

3 The Numerical Scheme

In this section, we lay out the numerical algorithm to solve the system (2.16), whereas in the next one, the physical parameters will be determined. For the mathematical analysis as well as for the numerical approximation, the system is transformed by $\tilde{u}(x,t) := u(x,t) - x \cdot m(t)$. Thus, we deal with homogeneous boundary conditions. An additional term $\rho \cdot x \cdot \ddot{m}(t)$ appears only on the left hand side of the momentum balance. For simplicity, the tilde is omitted. The results presented in the last section, of course, refer to the original problem.

We do need some notations. The mesh sizes and the time step size, respectively, are

$$h := \frac{1}{n_x}, \qquad \tilde{h} := \frac{1}{N}, \qquad N = n_x \cdot l, \tag{3.1}$$

$$k := \frac{T}{n_t}, \tag{3.2}$$

where $n_x, l, n_t \in \mathbb{N}$ and $n_x \geq 2$. Let $\mathcal{B}_{n_x}$ denote the set of cubic splines on $\overline{\Omega}$ and $x_i := \frac{i}{n_x}$, $i = -3, -2, \ldots, n_x+3$. Then the set of functions $\{B_{-3}, B_{-2}, B_{-1}, B_0, B_1, \ldots, B_{n_x-1}\}$

with

$$B_\nu(x) := \frac{1}{6h^3}\begin{cases} (x-x_\nu)^3 & , \quad x_\nu \le x < x_{\nu+1} \\ h^3+3h^2(x-x_{\nu+1}) & \\ +3h(x-x_{\nu+1})^2-3(x-x_{\nu+1})^3 & , \quad x_{\nu+1} \le x < x_{\nu+2} \\ h^3+3h^2(x_{\nu+3}-x) & \\ +3h(x_{\nu+3}-x)^2-3(x_{\nu+3}-x)^3 & , \quad x_{\nu+2} \le x < x_{\nu+3} \\ (x_{\nu+4}-x)^3 & , \quad x_{\nu+3} \le x < x_{\nu+4} \\ 0 & , \quad \text{else,} \end{cases} \tag{3.3}$$

defines a basis of $\mathcal{B}_{n_x} \subset H^3(\Omega)$. The set of functions $\{w_{-1}, w_0, w_1, \ldots, w_{n_x-3}\}$ with

$$w_i(x) := \begin{cases} B_{-1}(x) - B_{-3}(x) & , \quad i=-1 \\ B_i(x) & , \quad i=0,\ldots,n_x-4 \\ B_{n_x-3}(x) - B_{n_x-1}(x) & , \quad i=n_x-3, \end{cases} \tag{3.4}$$

defines a basis of $\mathcal{W}_{n_x} \subset H^3_E(\Omega) := \{\, u \in H^3(\Omega) \;\big|\; u(0)=u''(0)=u(1)=u''(1)=0 \,\}$. For the displacement u, the finite element ansatz

$$u^j(x) = \sum_{i=-1}^{n_x-3} v_i^j w_i(x), \quad 0 \le x \le 1, \tag{3.5}$$

is used, where $j = 0,\ldots,n_t$ denotes the time step and $v^j := (v^j_{-1}, v^j_0, \ldots, v^j_{n_x-3}) \in \mathbb{R}^{n_x-1}$. So, the first derivative with respect to space then reads

$$u^j_x(x) = \sum_{i=-1}^{n_x-3} v_i^j w_i'(x); \tag{3.6}$$

higher order derivatives are defined analogously. Furthermore, θ_i^j are approximate solutions for $\theta(i\cdot\tilde{h}, j\cdot k)$ and we define $\theta^j := (\theta_0^j, \theta_1^j, \ldots, \theta_N^j) \in \mathbb{R}^{N+1}$, $G_i^j := g(i\cdot\tilde{h}, j\cdot k)$, and $\theta_\Gamma^j := \theta_\Gamma(j\cdot k)$, $0 \le i \le N$, $0 \le j \le n_t$. The constants ρ, α, β, γ, δ, θ_1, c_e, κ, and $\overline{\kappa}$ have real values.
We introduce the projection

$$P_{n_x} := H^1(\Omega)\text{–orthogonal} \quad \text{projektion} \quad \text{onto} \quad \mathcal{W}_{n_x} \tag{3.7}$$

and consider the semi–discretized system:

Find $\left((u^j)_{j=-1}^{n_t}, (\theta^j)_{j=0}^{n_t}\right)$ such that

$$\int_0^1 \Big(\rho\Big(\frac{u^j(x)-2u^{j-1}(x)+u^{j-2}(x)}{k^2} + x\ddot{m}(j\cdot k)\Big)w_i(x) + \delta u^j_{xx}(x)w_i''(x)\Big)dx$$

$$+\int_0^1 \Big(\big(\hat\theta^{j-1}(x)-\theta_1\big)F_1'(\varepsilon^j(x))+F_2'(\varepsilon^j(x))\Big)\,w_i'(x)dx \;=\; 0,$$
$$\forall\, w_i\in\mathcal{W}_{n_x},\quad 0<j\le n_t, \tag{3.8a}$$

$$c_e\frac{\theta_i^j-\theta_i^{j-1}}{k}-\kappa\cdot\frac{\theta_{i+1}^j-2\theta_i^j+\theta_{i-1}^j}{\tilde h^2}-\gamma\left(\frac{(\varepsilon^j(i\cdot\tilde h))^2-(\varepsilon^{j-1}(i\cdot\tilde h))^2}{2k}\right)\theta_i^{j-1}=G_i^j,$$
$$0\le i\le N,\quad 0<j\le n_t, \tag{3.8b}$$

$$u^0=P_{n_x}(u_0),\quad \frac{u^0-u^{-1}}{k}=P_{n_x}(u_1)\equiv 0,\quad \theta^0=\theta_0(i\cdot\tilde h),\quad 0\le i\le N. \tag{3.8c}$$

Here we have $\theta_{-1}^j:=\theta_1^j$, $\theta_{N+1}^j:=\theta_{N-1}^j-2\tilde h\frac{\overline\kappa}{\kappa}(\theta_N^j-\theta_\Gamma^j)$, $\varepsilon^j(x):=u_x^j(x)+m(j\cdot k)$, $F_1'(\varepsilon)=\gamma\varepsilon$, and $F_2'(\varepsilon)=-\beta\varepsilon^3+\alpha\varepsilon^5$. $\hat\theta^j:\overline\Omega\to\mathbb{R}$ denotes the linear interpolating function to the grid points $(i\cdot\tilde h,\theta_i^j)$, $0\le i\le N$.
In (3.8) the equations are decoupled, and thus we first solve the discretized version of the momentum balance and then the one of the energy balance.
In order to deal with the nonlinearities of the momentum balance, we apply the ansatz developed in [NS] and we approximate:

$$\begin{aligned}
&(\hat\theta^{j-1}-\theta_1)F_1'(\varepsilon^j)+F_2'(\varepsilon^j)\\
&\approx\ (\hat\theta^{j-1}-\theta_1)\frac{1}{2}\gamma\frac{(\varepsilon^j)^2-(\varepsilon^{j-1})^2}{\varepsilon^j-\varepsilon^{j-1}}-\frac{1}{4}\beta\frac{(\varepsilon^j)^4-(\varepsilon^{j-1})^4}{\varepsilon^j-\varepsilon^{j-1}}+\frac{1}{6}\alpha\frac{(\varepsilon^j)^6-(\varepsilon^{j-1})^6}{\varepsilon^j-\varepsilon^{j-1}}\\
&=\ (\hat\theta^{j-1}-\theta_1)\frac{1}{2}\gamma(\varepsilon^j+\varepsilon^{j-1})-\frac{1}{4}\beta\sum_{k=0}^{3}(\varepsilon^j)^{3-k}(\varepsilon^{j-1})^k+\frac{1}{6}\alpha\sum_{k=0}^{5}(\varepsilon^j)^{5-k}(\varepsilon^{j-1})^k.
\end{aligned} \tag{3.9}$$

So, the momentum balance at grid point i reads:

$$\begin{aligned}
0\ =\ &\rho\frac{1}{k^2}\sum_{\nu=-1}^{n_x-3}(v_\nu^j-2v_\nu^{j-1}+v_\nu^{j-2})\cdot\int_0^1 w_\nu(x)w_i(x)dx+\rho\ddot m(j\cdot k)\cdot\int_0^1 xw_i(x)dx\\
&+\delta\sum_{\nu=-1}^{n_x-3}v_\nu^j\cdot\int_0^1 w_\nu''(x)w_i''(x)dx\\
&+\int_0^1\Big(\ \frac{\gamma}{2}(\hat\theta^{j-1}(x)-\theta_1)(\varepsilon^j(x)+\varepsilon^{j-1}(x))\\
&\qquad-\frac{\beta}{4}\sum_{k=0}^{3}(\varepsilon^j(x))^{3-k}(\varepsilon^{j-1}(x))^k+\frac{\alpha}{6}\sum_{k=0}^{5}(\varepsilon^j(x))^{5-k}(\varepsilon^{j-1}(x))^k\ \Big)\,w_i'(x)dx\\
=:\ &H_i(v_{-1}^j,\dots,v_{n_x-3}^j),
\end{aligned} \tag{3.10}$$

where $H:\mathbb{R}^{n_x-1}\to\mathbb{R}^{n_x-1}$. We solve this equations using a Newton method.
Each interval of length h is subdivided into l subintervals (see (3.1)). We calculate the integrals over these subintervals. In case there occur only cubic splines in the

integrals, they can be evaluated analytically. Otherwise, we make use of the extended trapezoidal rule for numerical evaluation. One has to evaluate the integrals only where the supports of the cubic splines do not vanish, i.e. if $i-3 \leq \nu \leq i+3$. We use a Householder transformation and exploit symmetries.
For the discretized energy balance, after invoking the boundary conditions, we end up with a linear system $A\vec{x}^j = \vec{b}^j$ which is solved with the help of a standard LU decomposition.

4 The physical parameters

In this section, we determine the parameters for the specimen used by Glasauer in his experiments [GL]. He obtained the load–deformation diagrams shown in Figures 6.a–e (the temperature increases from Figure 6.a to 6.e). The elongation was prescribed, and the necessary load for that elongation was measured. We want to compare the experimental load at the elongated side with the stress inside the rod (2.8) at the right boundary which can be calculated numerically. The stress at the right boundary of the rod ($x = 1$) is equal to the pressure from outside, that is

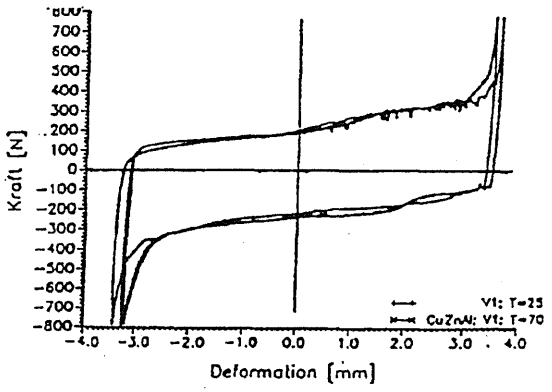

Figure 6.a

$$\sigma(1,t) = \frac{F(t)}{A(t)}, \tag{4.1}$$

at any time t. $F(t)$ is the measured load, $A(t)$ denotes the time–dependent cross–section of the rod. No volume change is considered, so we have

$$A_0 \cdot \Delta x_0 = A(t) \cdot \Delta x(t). \tag{4.2}$$

A_0 is the cross-section of the rod without any elongation, Δx_0 denotes the length of a small volume element at the right boundary at this time, $\Delta x(t)$ denotes that length at time t. A_0 is known, and thus one has

$$\begin{aligned}\sigma(1,t) &= \frac{F(t) \cdot \Delta x(t)}{A_0 \cdot \Delta x_0} \\ &= \frac{F(t)}{A_0} \cdot \frac{1 + u(1,t) - ((1-\Delta x_0) + u(1-\Delta x_0, t))}{\Delta x_0}\end{aligned}$$

$$= \frac{F(t)}{A_0} \cdot \frac{\Delta x_0 + u(1,t) - u(1-\Delta x_0, t)}{\Delta x_0}$$

$$\longrightarrow \quad \frac{F(t)}{A_0} \cdot (1 + u_x(1,t)), \qquad \Delta x_0 \to 0. \tag{4.3}$$

As mentioned in the introduction, we have to determine α, β, γ, and θ_1. θ_1 can easily be found with the help of the experimental results [MÜ]. For simplicity (which will not be done in calculating σ in the next section), we set $1 + u_x(x,t) \approx 1$, the error will be less than 9%. Using graphical approximation and the least squares fitting, we are able

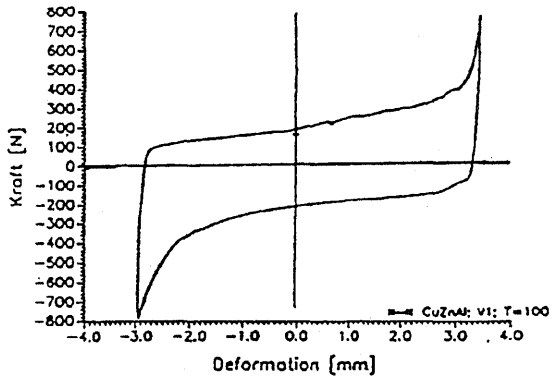

Figure 6.b

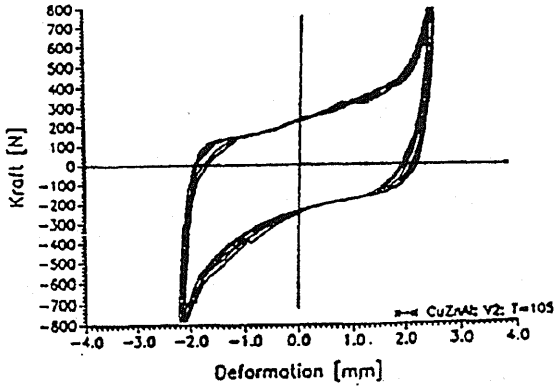

Figure 6.c

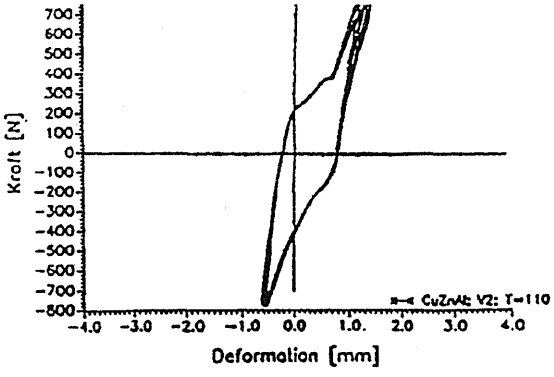

Figure 6.d

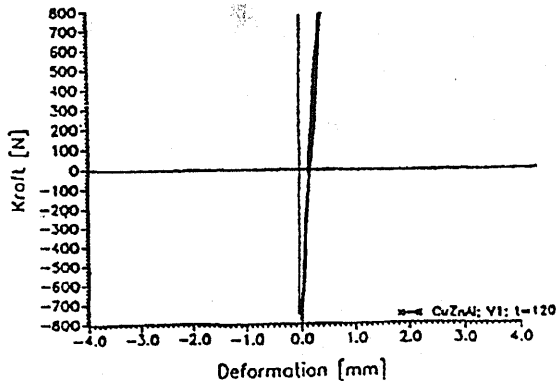

Figure 6.e

to determine the material constants. The areas inside the experimental hysteresis loops do not differ more than 10% from the theoretical ones. The theoretical curve does not comply with the experimental one in the first of the five diagrams (Figure 6.a: lowest temperature). In a Landau–Devonshire model, the hysteresis loops always grow with decreasing temperature. In the experiments, however, one does not observe a growth of the hysteresis loops below a certain temperature. So, below this temperature, a Landau–Devonshire ansatz looses its validity. Furthermore, we remark that, if the

constants depended on the temperature, we would be able to fit the parameters nearly perfectly.

The values for ρ and c_e are taken from [FHM] because it is the same material. The values for κ and δ are the same as in [KL], and $\overline{\kappa}$ is chosen as big as necessary to simulate a bath at the right boundary. Altogether, we have the following values:

$$\begin{aligned}
&\alpha = 2.49 \cdot 10^8 \frac{\mathrm{J}}{\mathrm{cm}^3}, && \rho = 8.23 \frac{\mathrm{g}}{\mathrm{cm}^3},\\
&\beta = 2.343 \cdot 10^6 \frac{\mathrm{J}}{\mathrm{cm}^3}, && c_e = 3.1274 \frac{\mathrm{J}}{\mathrm{cm}^3\mathrm{K}},\\
&\gamma = 190.18 \frac{\mathrm{J}}{\mathrm{cm}^3\mathrm{K}}, && \kappa = 2.39 \frac{\mathrm{W}}{\mathrm{cmK}},\\
&\delta = 2.0 \cdot 10^{-10} \frac{\mathrm{J}}{\mathrm{cm}}, && \overline{\kappa} = 10^9 \frac{\mathrm{W}}{\mathrm{cm}^2\mathrm{K}},\\
&\theta_1 = 348.75\,\mathrm{K}. &&
\end{aligned} \tag{4.4}$$

The other quantities have the following units:

$$[u] = [m] = \mathrm{cm}, \quad [u_x] = 1, \quad [u_{tt}] = \frac{\mathrm{cm}}{\mathrm{sec}^2}, \quad [u_{xxxx}] = \mathrm{cm}^{-3}. \tag{4.5}$$

In the beginning (no elongation), the specimen has a length of $l_0 = 3.4 \cdot 10^{-2}$ m, and a cross–section of $A_0 = 4.5 \cdot 10^{-6}\mathrm{m}^2$. We choose as units $\frac{100\ \mathrm{N}}{\mathrm{cm}^3}$ for the momentum balance, and $\frac{\mathrm{J}}{\mathrm{cm}^3\mathrm{sec}}$ for the energy balance.

5 Numerical simulations

For all simulations, we have an initial temperature θ_0 in the entire rod, and a surrounding temperature θ_Γ of 373.1 K. This corresponds to Figure 6.b. With the parameters of the foregoing section, the free energy shows, at this temperature, three minima: The two variants of martensite are stable, as well as austenite. Thus, we have the case of a state between the two states shown in Figures 3 and 4. The resulting stress–strain relation still exhibits a quasiplastic hysteresis. Furthermore, the parameter l (3.1) is always chosen so that $N = 600$. The time step size $k = \frac{T}{n_t}$ varies between $5 \cdot 10^{-8}$s and 10^{-7}s. All other parameters have the values given in (4.4) or in the foregoing simulation, respectively.[3]

Simulation 1: length of cycle: $T = 0.5$ s

[3]All simulations were done on a *digital* DEC 3000 600–Workstation (187 SPECfp92).

time step size: $k = 10^{-7}$ s

no. of grid points (momentum balance): $n_x = 24$

maximal elongation: $m_0 = 0.088$ cm (5.1)

The initial state is:

$$0 \leq x \leq 0.25 \ : \ M_+,$$
$$0.25 \leq x \leq 0.75 \ : \ M_-,$$
$$0.75 \leq x \leq 1.0 \ : \ M_+.$$

This complies with the boundary conditions and the rod has a vanishing resulting displacement. The cycle consists of five parts of equal length: first, the rod is pulled till m_0; this is called the initial loading path in the stress–elongation diagrams (SED). Then, the cycle itself starts: the rod is pushed back to zero and further to $-m_0$. Afterwards, it is pulled back to zero again, and is moved to m_0. In Figure 7, the displacement u in the rod is plotted in the course of time. The rod is shown on the x–axis: at $x = 0$, we have the left end of the rod where it is clamped; at $x = 1$, we have the right end where we have the heat exchange with the surrounding temperature, and where the rod is elongated. The y–axis shows the time. Since $u(1,t) = m(t)$,

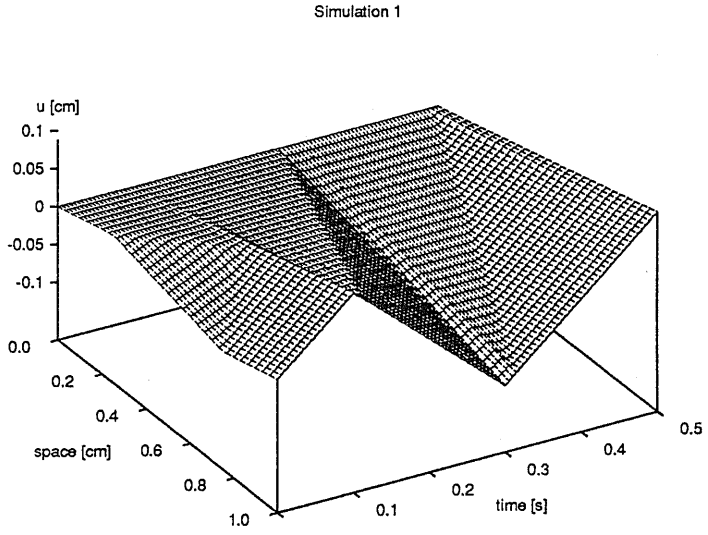

Figure 7: Simulation 1: displacement u

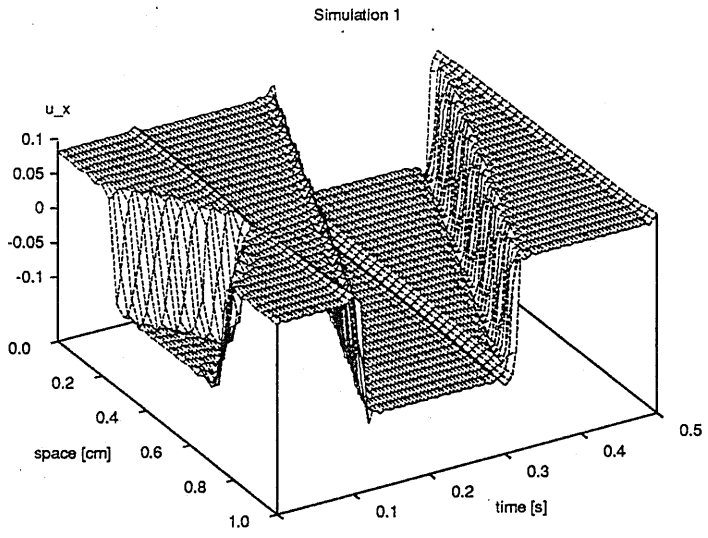

Figure 8: Simulation 1: strain u_x

we can see the curve $(t, m(t))$ at $x = 1$. At $t = 0$, the initial state u_0 can be seen. In the same way, we have plotted the strain u_x in Figure 8. One clearly sees the two boundaries at $t = 0$ which start moving towards each other until the whole rod exhibits the $M+$–phase. Then, pushing the rod back to $m = -m_0$ causes one phase boundary propagating through the rod which has started at $x = 1$. The rod, at that time, only shows the $M-$–phase. Pulling the rod back leads again to one phase boundary starting at $x = 1$ and ends up with only one phase, i.e. $M+$. It depends sensitively on the parameters how the phases develop in the course of time. The behaviour depends, e.g., on the way of pulling and pushing or whether there is a heat exchange or not. For instance, it is possible to obtain a development of the phases which has the form of a "V" instead of a "corridor" or more than one phase boundary. We will see this in some of the next simulations.

In Figure 9, the temperature evolution is shown. One observes the temperature increasing and decreasing due to the phase transitions. We explain this in the following. In a transition from one martensite variant to the other, one particle describing the system (i.e. one grid point), coming out of its metastable minimum of potential energy, has to overcome a little potential barrier in order to fall into the deeper global minimum of potential energy.[4] Thus, first kinetic energy is transformed into potential energy (the particle climbs up the barrier), one observes a decrease in temperature. When the particle falls down into the global minimum, potential energy is transformed into kinetic energy: the temperature increases. In Figure 8, one can see that a grid point needs approximately 8 time intervals to change its phase. Plotting only every 50.000th time step, we see that a grid points needs 400.000 time steps for a phase transition. Thus,

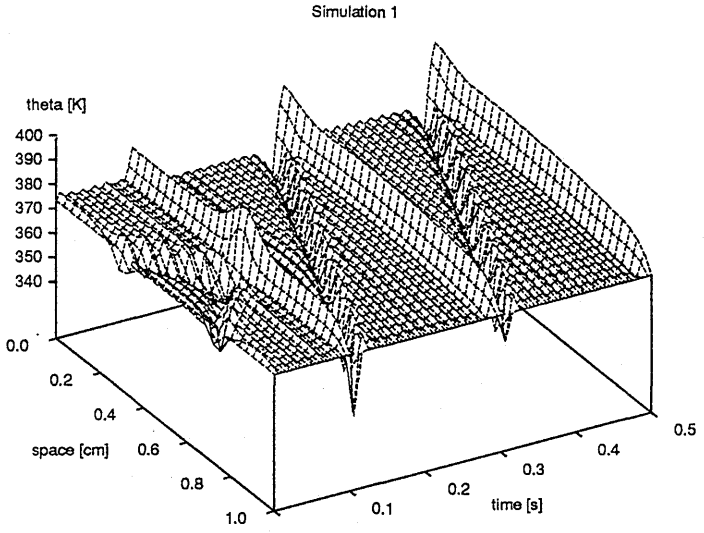

Figure 9: Simulation 1: temperature θ

[4]When there is no force acting on the rod, the two minima of the martensite variants are, of course, of the same depth. In the current case, austenite does not occur although it is stable and, for simplicity, we only focus on the transition between the two martensite minima.

we are able to see how the temperature decreases and increases.
Therefore, we have the following temperature profile for a phase transition from one martensite structure to the other: there is a heat sink followed by a pole of heat. This temperature profile is moving together with the phase boundary. Thus, we explain the temperature distribution in Figure 9. To make the picture clear, we have plotted the temperature distribution θ again at $t = 0.05$ s in Figure 10. We see the discussed temperature profile twice coming from both ends to the middle of the rod, together with the two phase boundaries. At this time, the phase boundaries have nearly merged. Due to the boundary conditions ($x = 0$: isolated end; $x = 1$: heat exchange with the surrounding temperature $\theta_\Gamma = 373.1$ K $= \theta_0$), the temperature at the left end has increased, whereas at the right boundary, the corresponding heat could flow out, and we have $\theta = 373.1$ K at $x = 1$.

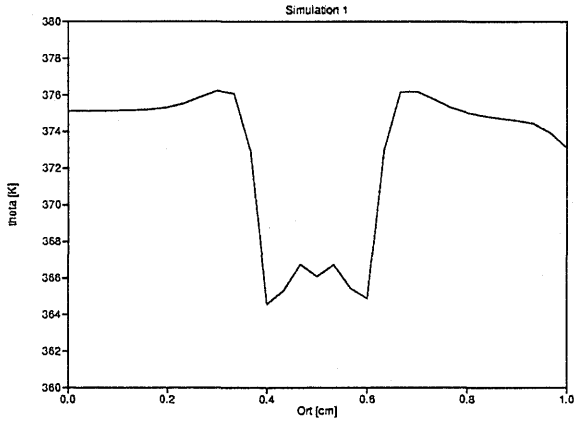

Figure 10: Simulation 1: θ at $t = 0.05$ s

One observes differences in temperature of more than 20 K. These are no realistic values, but we obtain differences of less than 5 K by choosing cycle lenghts $T \geq 2.0$ s. This coincides with the experiments [MÜ]. Since our calculations do take up to 5 weeks on our workstation (depending on the number of grid points), we have chosen such a short cycle because all relevant phenomena occur at least qualitatively. The big increase of temperature at the turning points of m are due to numerical effects.
In a second simulation (Figures 11 to 13) we have only austenite in the beginning.

$$\begin{aligned} \textbf{Simulation 2:} \quad & T = 1.0 \text{ s} \\ & k = 5 \cdot 10^{-8} \text{ s} \\ & m_0 = 0.0812 \text{ cm} \\ & \overline{\kappa} = 0 \end{aligned} \tag{5.2}$$

Now the rod is pulled and pushed in a different way: at the turning points of m, it lingers for some time which can be seen in Figure 11. In Figure 12, one observes, in the first part of the cycle, that the rod first behaves elastically and then there is a transition to $M+$ at random positions which spread out until the entire rod exhibits the $M+$-phase. We think that this nucleation process, which is observed in the experiments, is due to rounding errors of the computer. We obtain this behaviour in the course of the whole cycle and we see, in contrast to the foregoing simulation, that austenite occurs

during the transition from one martensite structure to the other.

The temperature evolution (Figure 13) shows very well the latent heats at points where a phase transition takes place: the temperature increases when going from austenite to one martensite variant, it decreases going the opposite direction.

In the following, we will focus on SED's. The stress at the right boundary $stress(1,t) := \sigma(1,t)/(1+u_x(1,t))$ (see (4.3)) is plotted over the elongation $m(t)$. Figure 14 shows this for simulation 1. After the initial loading path ($m = 0$ to $m = m_0$) we find a hysteresis. Pushing the rod leads to negative stress, pulling to positive. The big fluctuations at the turning points of m are due to the above mentioned numerical effects.

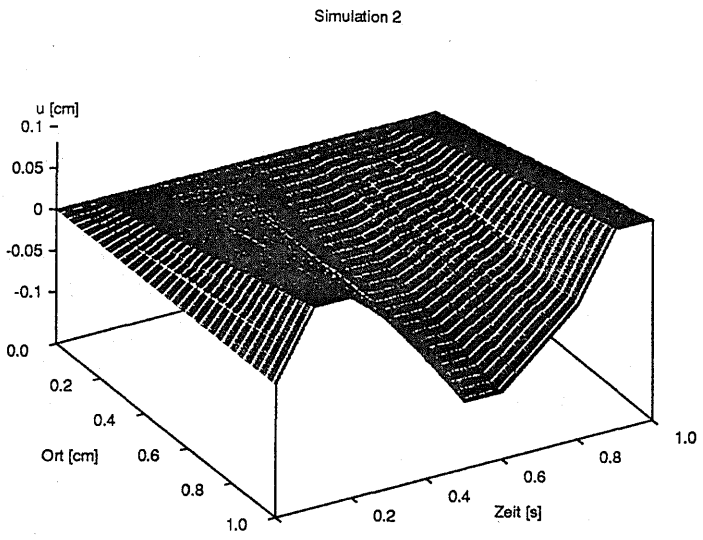

Figure 11: Simulation 2: displacement u

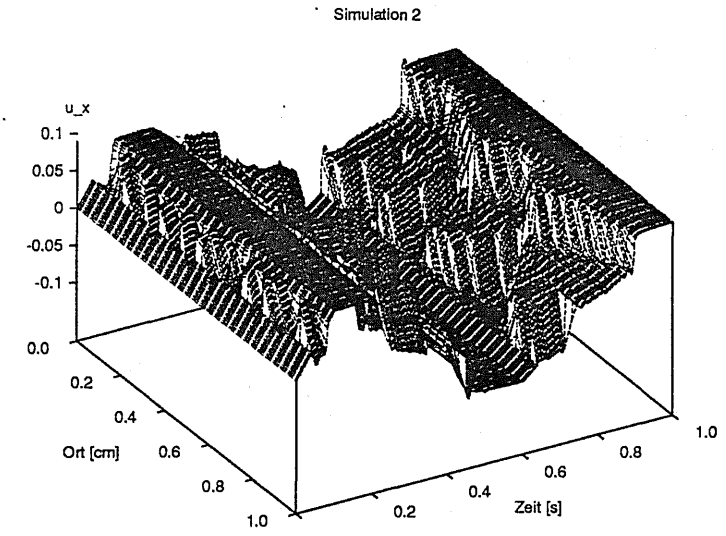

Figure 12: Simulation 2: strain u_x

The smaller fluctuations between the turning points correspond to the number of grid points. Every phase change of a grid point leads to a small oscillation. Such effects are also observed in [MV].

In order to get rid of these oscillations or, at least, to smoothen the hysteresis, we take more grid points in the momentum balance.

Simulation 3: $n_x = 50$ (5.3)

Simulation 4: $n_x = 100$ (5.4)

Looking into Figures 14 to 16, one finds out that the hysteresis vanishes: it is due to a numerical effect. So, thinking that the Ginzburg–coefficient given by Falk is a lot too small in order to model the energy between the phases, we choose bigger values for δ. We find that with $\delta = 2 \cdot 10^{-1}$ J/cm (for 24 grid points) the stress–strain relation starts to change. Taking $\delta = 1.0$ J/cm, we have a much better hysteresis; choosing δ even bigger than that, the resulting behaviour makes no sense any more. Figures 17 to 19 show the same simulations again but with $\delta = 1.0$ J/cm:

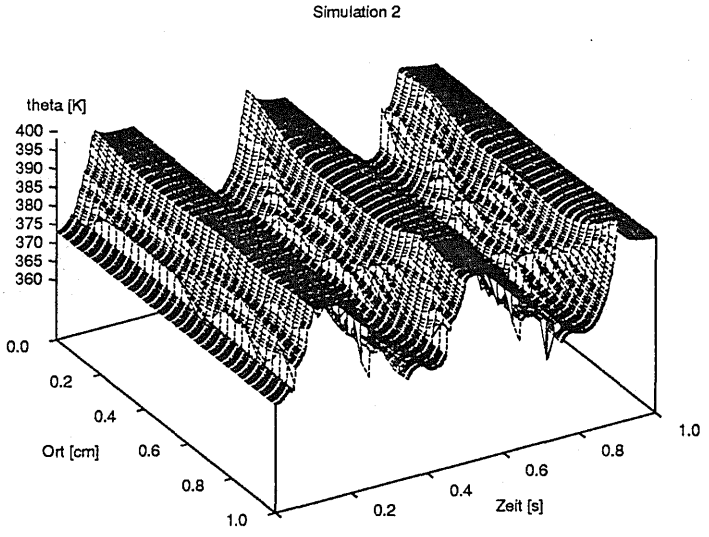

Figure 13: Simulation 2: temperature θ

Simulation 5: $\delta = 1.0$ J/cm, $n_x = 24$ (5.5)

Simulation 6: $\delta = 1.0$ J/cm, $n_x = 50$ (5.6)

Simulation 7: $\delta = 1.0$ J/cm, $n_x = 100$ (5.7)

Now, we find a hysteresis which is stable concerning discretization. More grid points give a smoother hysteresis loop which one would expect naturally. There are still some fluctuations at the turning points of m which are caused by the above mentioned numerical effects (see Figure 9). To get rid of them, one would have to choose another numerical scheme.

This difference in the stress–strain relation for such different values of δ can be confirmed in the next two simulations. All the parameters are the same as in the simulations 1 and 5, respectively, except for the cycle length:

Simulation 8: $\delta = 2 \cdot 10^{-10}$ J/cm, $T = 2.0$ s (5.8)

Simulation 9: $\delta = 1.0$ J/cm, $T = 2.0$ s (5.9)

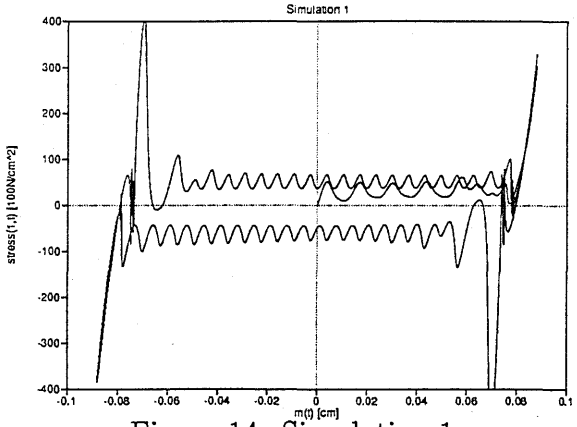

Figure 14: Simulation 1
$\delta = 2 \cdot 10^{-10}$ J/cm, 24 grid points

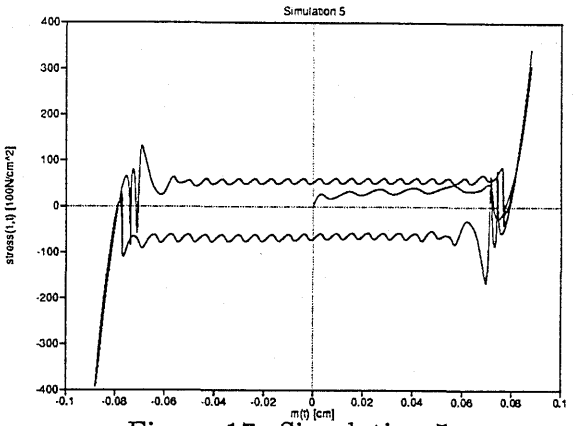

Figure 17: Simulation 5
$\delta = 1.0$ J/cm, 24 grid points

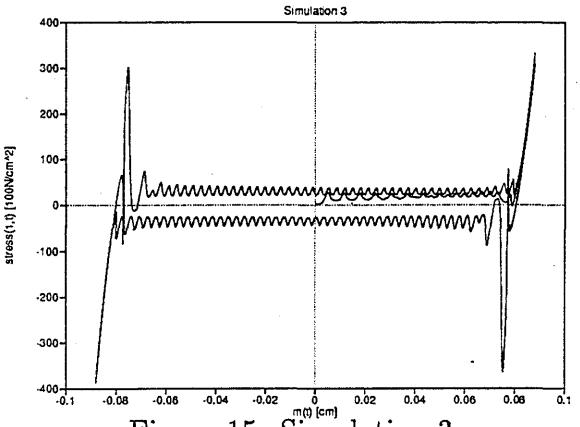

Figure 15: Simulation 3
$\delta = 2 \cdot 10^{-10}$ J/cm, 50 grid points

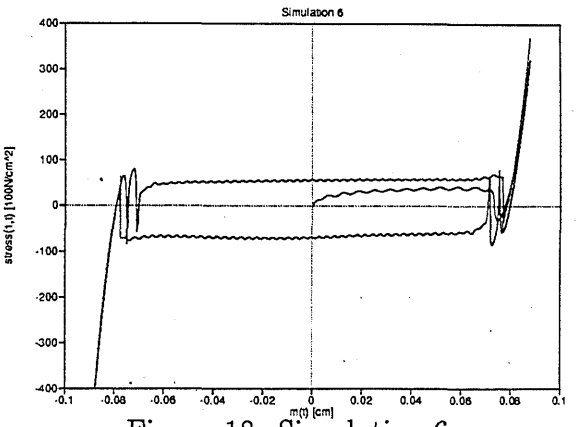

Figure 18: Simulation 6
$\delta = 1.0$ J/cm, 50 grid points

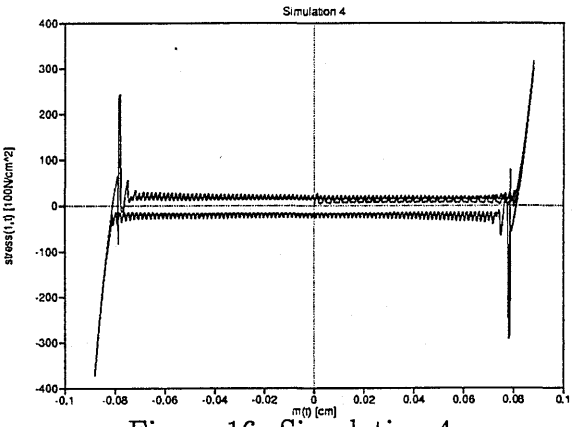

Figure 16: Simulation 4
$\delta = 2 \cdot 10^{-10}$ J/cm, 100 grid points

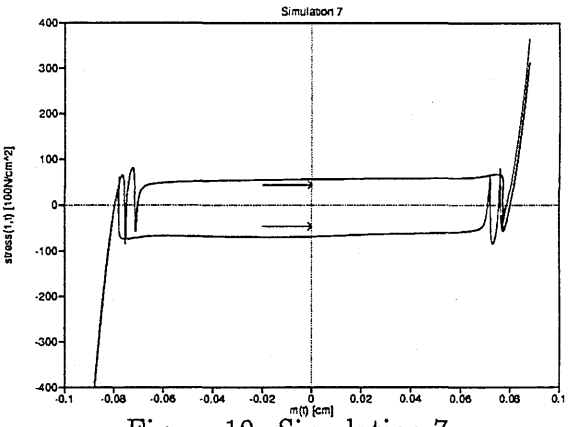

Figure 19: Simulation 7
$\delta = 1.0$ J/cm, 100 grid points

Simulation 8 (Figure 20) shows again that the hysteresis loop vanishes, this time, because the velocity of pushing and pulling decreases. In simulation 9 (Figure 21), the hysteresis is also partly vanishing but this is due to another reason: As we have

mentioned above, the time evolution of the phases may change even though the change in parameters is small. Here, we observe that the evolution is different than in all the others before; up to now, they have always been as in Figure 8. In this simulation, we have martensite at the right end only around the turning points. Austenite is stable, so it is "allowed" to occur. So, where the loop is smaller, now, it is due to the fact that we have austenite instead of martensite. This is clearly to be seen, of course, plotting $u_x(x,t)$ for this simulation (which is not shown here). The hysteresis loop is as big as in simulation 5, where we have martensite as before; this can be seen around the turning points of m in Figure 21.[5] So, we find that the hysteresis is rate independent, if δ is big enough.

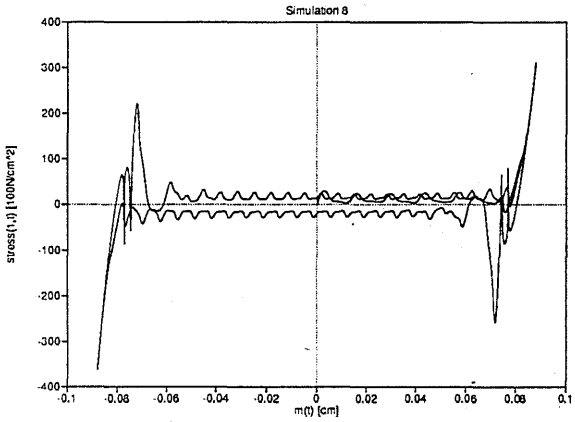

Figure 20: Simulation 8
$\delta = 2 \cdot 10^{-10}$ J/cm, $T = 2.0$ s

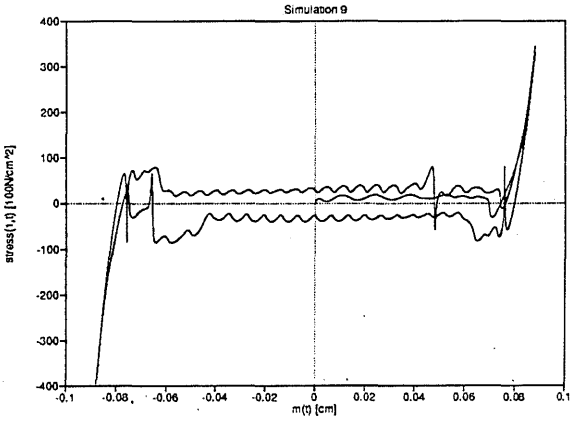

Figure 21: Simulation 9
$\delta = 1.0$ J/cm, $T = 2.0$ s

Summarizing, we have the following result: The small value $\delta = 2 \cdot 10^{-10}$ J/cm leads to a hysteresis which depends on the discretization and which is not rate independent. In this case, one finds the Maxwell line which one would have expected for a pure Landau–Devonshire model: $\delta = 0$. Choosing the Ginzburg–coefficient big enough, we end up with a hysteresis that does not depend on the discretization and that is rate independent. In this case, we even find quantitative agreement with the experiment (Figure 6b and 19: the arrows in Figure 19 indicate the size of the experimental loop at $m = 0$. Since $stress(1,t) = F(t)/A_0$, one has to divide the values for the load by $A_0 = 4.5 \cdot 10^{-6}\text{m}^2$; furthermore, the y–axis is shown too far left in Figure 21. The length of the rod is 3.4 cm, in our simulation, we have $l = 1$ cm.)
The hysteresis can be seen even more clearly plotting $u_x(1,t)$ over $m(t)$ (Figure 22; here: Simulation 7). The polynom $\sigma(1,t)$, underlying the Landau–Ginzburg model, is

[5]This is an example where the simulation basing on this model for the dynamical behaviour does not completely comply with the quasistatic behaviour; for another example we refer to [BU].

shown in Figure 23 (simulation 5). The expected transitions according to this diagram agree with the corresponding SED.

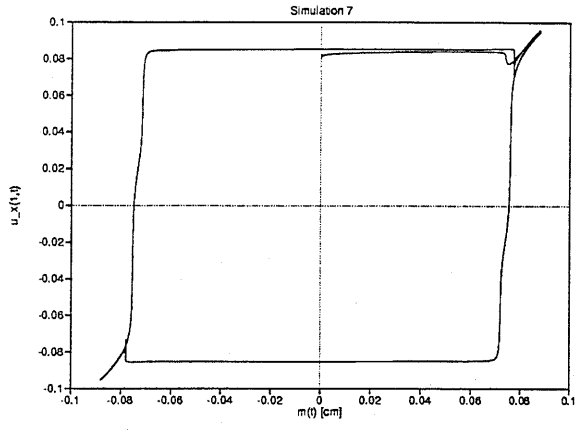

Figure 22: strain at $x = 1$

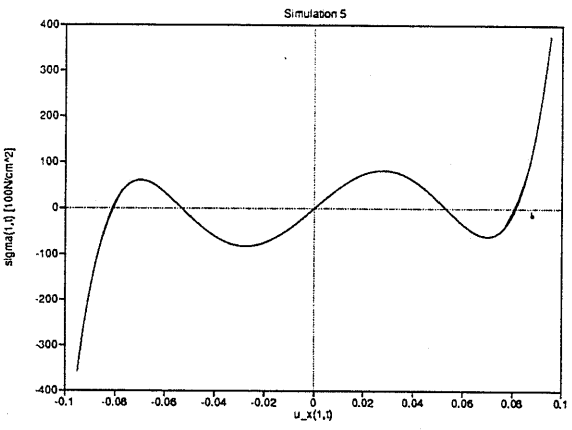

Figure 23: $\sigma(1,t)$ over $u_x(1,t)$

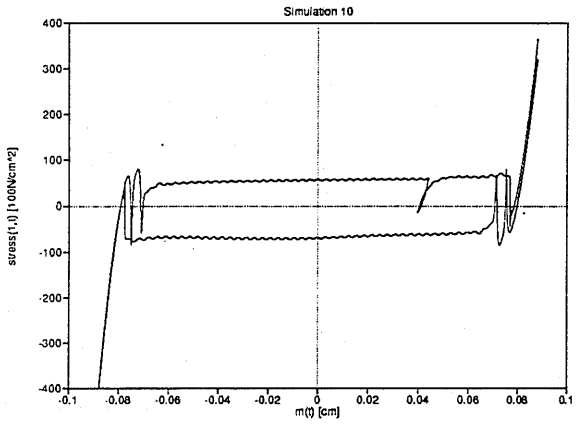

Figure 24: Short interruption of the cycle

The following simulations show the stress–strain relation inside the hysteresis loop. All parameters are the same as in simulation 6, except for the form of $m(t)$. This can easily be seen in the diagrams. Simulation 10 (Figure 24) shows that the rod behaves elastically if one interrupts the cycle (here, it is shown in the last part of the cycle), pushes the rod a little bit back and continues then the cycle as before.[6] This behaviour is also observed experimentally [MÜ]. In Figures 25 and 26, we compare inner loops found in the experiments by Glasauer [GL] and numerical simulated ones. Here, we have good agreement in the lower part of the loops and less good agreement in the upper part. The temperature is slightly different.
Altogether, we sum up with the three following features:

- The simulations, i.e. displacement, strain and temperature evolution show the experimentally observed phenomena: Phase transitions between variants of martensite or between austenite and one variant, respectively, changes of temperatures and latent heats, nucleation processes, moving and propagation of phase boundaries.

[6]The velocity of the pushing and pulling does not change in one simulation.

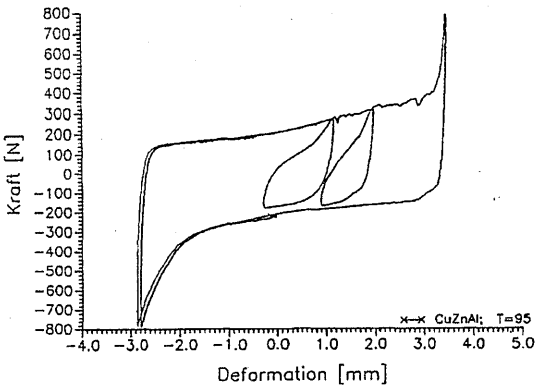

Figure 25: Interior loops [GL]

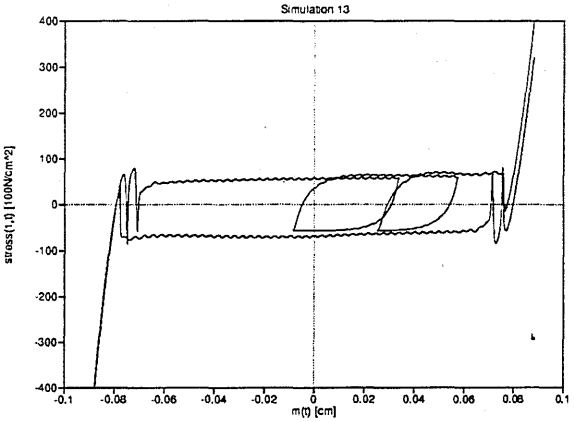

Figure 26: Simulation 13

- We find that the coefficient of the term modelling the interfacial energy determines the size of the loop. There is a value for this Ginzburg–coefficient leading to quantitative agreement with the experiment. This corresponds with the ansatz of [FHM]: They introduce a coherency energy which depends on the number of interfaces. The coefficient of this term is proportional to the size of the hysteresis loop. Thus, the connection between the ansatz of [FHM] and a nonlocal one for the interfacial energy as it has been found out by Rogers [RO] is confirmed by our numerical investigation. One has to consider another derivation of the value for δ than the one given by Falk [FA2].

- For the first time, we have numerical simulations of the inner structure of a hysteresis loop. Qualitatively, the simulations comply in parts with the experiments. We find loops having the form of "drops" which can also be found in ferromagnetism (see [MA]). On the other hand, we are not able to simulate interior loops which indicate the existence of the phase equilibrium line which is also part of the ansatz of [FHM] or [WIL], respectively. This line goes from the upper left corner to the lower right one of the outer loop. The stress–strain behaviour always changes when coming to this line. The phase equilibrium line is observed in most of the experiments (see Figure 27). One possible explanation could be that these experiments only refer to the pseudoelastic range

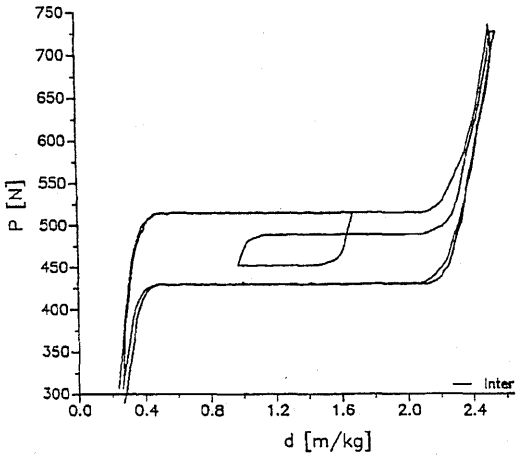

Figure 27: Interior loops [FHM]

while our simulations concern the quasiplastic one. We are now investigating the pseudoelastic range.

Acknowledgement

The author wishes to express his gratitude to Prof. Dr. J. Sprekels and to Prof. Dr. I. Müller for their support of this work. Furthermore, he has to thank Dr. D. Hömberg and O. Klein for many discussions.

References

[BU] Bubner, N., *Modellierung dehnungsgesteuerter Phasenübergänge in Formgedächtnislegierungen,* Dissertation Universität GH–Essen, Verlag Shaker, Aachen, 1995.

[FA1] Falk, F., *Landau Theory and Martensitic Phase Transitions,* Journal de Physique **C4** (1982) 3–15.

[FA2] Falk, F., *One–dimensional model of shape memory alloys,* Archives of Mechanics **35** (1983) 63–84.

[FA3] Falk, F., *Elastic Phase Transitions and Nonconvex Energy Functions.* In: "Free Boundary Problems: Theory and Applications I" (K.–H. Hoffmann, J. Sprekels, eds.), Longman, London, 1990.

[FHM] Fu, S., Huo, Y., Müller, I., *Thermodynamics of pseudoelasticity – an analytical approach,* Acta Mechanica **99** (1993) 1–19.

[GL] Glasauer, U., Dissertation TU Berlin, in preparation.

[HM] Huo, Y., Müller, I., *Nonequilibrium Thermodynamics of Pseudoelasticity,* Continuum Mechanics and Thermodynamics **5** (1993) 163–204.

[KL] Klein, O., *Stability and Uniqueness Results for a Numerical Approximation of the Thermomechanical Phase Transitions in Shape Memory Alloys,* Advances in Mathematical Sciences and Applications **5** (1995) 91–116.

[MA] Mayergoyz, I.D., *Mathematical Models of Hysteresis,* Springer–Verlag, Berlin, 1991.

[MM] Magnus, H., Müller, H.H., *Grundlagen der Technischen Mechanik,* Teubner Verlag, Stuttgart, 1982.

[MÜ] Müller, I., private communication, 1994.

[MV] Müller, I., Villaggio, P., *A Model for an Elastic–Plastic Body,* Archive for Rational Mechanics and Analysis **65** (1979) 25–46.

[NS] Niezgódka, M., Sprekels, J., *Convergent numerical approximations of the thermomechanical phase transitions in shape memory alloys,* Numerische Mathematik **58** (1991) 759–778.

[RO] Rogers, R., *Some Remarks on Nonlocal Interactions and Hysteresis in Phase Transitions,* ICAM report 93–09–02, Virginia Polytechnic Institute and State University, Blacksburg, 1993.

[SP] Sprekels, J., *Shape Memory Alloys: Mathematical Models for a Class of First Order Solid–Solid Phase Transitions in Metals,* Control and Cybernetics **19** (1990) 287–308.

[STO] Stojanović, R., *Nonlinear Thermoelasticity,* Springer–Verlag, Wien – New York, 1972.

[WIL] Wilmanski, K., *Symmetric Model of Stress–Strain Hysteresis Loops in Shape Memory Alloys,* International Journal of Engineering Sciences **31** (1993) 1121–1138.

Recent publications of the Weierstraß–Institut für Angewandte Analysis und Stochastik

Preprints 1995

142. Johannes Elschner, Youngmok Jeon, Ian H. Sloan, Ernst P. Stephan: The collocation method for mixed boundary value problems on domains with curved polygonal boundaries.

143. Johannes Elschner, Ernst P. Stephan: A discrete collocation method for Symm's integral equation on curves with corners.

144. Dietmar Hömberg: A numerical simulation of the Jominy end–quench test.

145. Sabine Hengst: On the existence of classical solutions for a two phase flow through saturated porous media.

146. Anton Bovier, Véronique Gayrard: An almost sure large deviation principle for the Hopfield model.

147. Hans Babovsky: Limit theorems for deterministic Knudsen flows between two plates.

148. Björn Sandstede: Stability of multiple–pulse solutions.

149. Björn Sandstede: Constructing dynamical systems possessing homoclinic bifurcation points of codimension two.

150. Boris N. Khoromskij, Siegfried Prössdorf: Multilevel preconditioning on the refined interface and optimal boundary solvers for the Laplace equation.

151. Anton Bovier, Christof Külske: There are no nice interfaces in 2+1 dimensional SOS–models in random media.

152. Ilja Schmelzer: Covariant geometry description.

153. Alexander Korostelev, Michael Nussbaum: Density estimation in the uniform norm and white noise approximation.

154. Peter Hall, Michael Nussbaum, Steven E. Stern: On the estimation of a support curve of indeterminate sharpness.

155. Lev D. Pustyl'nikov: On the stability of solutions and absence of Arnol'd diffusion in a nonintegrable Hamiltonian system of a general form with three degrees of freedom.

156. Ralf Kornhuber: Adaptive monotone multigrid methods for some non–smooth optimization problems.

157. Sergej Rjasanow, Wolfgang Wagner: A generalized collision mechanism for stochastic particle schemes approximating Boltzmann type equations.

158. Nikolai Nefedov, Klaus Schneider: Singularly perturbed systems: Case of exchange of stability.

159. Rainer Dahlhaus, Michael H. Neumann, Rainer von Sachs: Nonlinear wavelet estimation of time–varying autoregressive processes.

160. Henri Schurz: Numerical regularization for SDEs: Construction of nonnegative solutions.

161. Anton Bovier, Véronique Gayrard: The retrieval phase of the Hopfield model: A rigorous analysis of the overlap distribution.

162. Boris N. Khoromskij, Gunther Schmidt: A fast interface solver for the biharmonic Dirichlet problem on polygonal domains.

163. Michael H. Neumann: Optimal change–point estimation in inverse problems.

164. Dmitry Ioffe: A note on the extremality of the disordered state for the Ising model on the Bethe lattice.

165. Donald A. Dawson, Klaus Fleischmann: A continuous super–Brownian motion in a super–Brownian medium.

166. Norbert Hofmann, Peter Mathé: On quasi–Monte Carlo simulation of stochastic differential equations.

167. Henri Schurz: Modelling, analysis and simulation of stochastic innovation diffusion.

168. Annegret Glitzky, Rolf Hünlich: Energetic estimates and asymptotics for electro–reaction–diffusion systems.

169. Pierluigi Colli, Jürgen Sprekels: Remarks on the existence for the one–dimensional Frémond model of shape memory alloys.

170. Klaus R. Schneider, Adelaida B. Vasil'eva: On the existence of transition layers of spike type in reaction–diffusion–convection equations.